Experimental and Numerical Characterization of H.S.S. Rotational Capacity

Elsy Saloumi[1], Marielle Hayeck[2], Joanna Nseir[3], Nicolas Boissonnade[4]

Abstract

The present paper is dedicated to the experimental characterization of hollow section shapes' rotational capacity. The purpose of the research works dealt with herein is to establish a direct dependence of the rotation capacity R_{cap} to a newly defined cross-sectional overall slenderness λ_{CS}. In other words, the intention is here to investigate how ductility can be associated with cross-section slenderness, in the perspective of providing designers with guidance on when allowed/not allowed to resort to plastic analysis and design.

The paper describes a series of bending tests that aimed at characterizing experimentally the relationship between ductility (R_{cap}) and cross-section compactness (λ_{CS}). Besides, numerical F.E. models created in the purpose of being substituted to physical tests are described, and tested against the experimental results. The F.E. models were shown capable of nicely replicating the experimental behavior of H.S.S. beams. Therefore, they can safely be substituted to physical tests and be subsequently used in extensive numerical studies, which are currently under development.

1. Introduction

The present paper is dedicated to the experimental characterization of hollow section shapes' rotational capacity. The purpose of the research works dealt with herein is to establish a direct dependence of the rotation capacity R_{cap} to a newly defined cross-sectional overall slenderness λ_{CS}, in addition to other parameters. In other words, the intention is here to investigate how ductility can be associated with cross-section slenderness, in the perspective of providing designers with guidance on when allowed/not allowed to resort to plastic analysis and design.

The basic idea developed in the present paper consists in an extended use of this λ_{CS} factor to define two families of sections:

- Sections allowing for plastic analysis and design ("class 1" sections, possessing sufficient rotational capacity for a plastic failure mechanism to develop);

---

[1] PhD, <elsysaloumi@gmail.com>
[2] PhD, <marielle_hayeck@hotmail.com>
[3] Professor, Saint-Joseph University, ESIB, <joanna.nseir@usj.edu.lb>
[4] Professor, Laval University, <nicolas.boissonnade@gci.ulaval.ca>

▪ Other sections for which the extent of local buckling precludes the attainment of sufficient ductile deformation for the development of a full plastic mechanism, so that plastic analysis is to be avoided.

In this respect, the target is to identify limit values of λ_{CS} as a function of key parameters so as to replace the R_{dem} vs. R_{cap} criterion (see Fig. 1), where R_{dem} is the rotation demand and R_{cap} is the rotation capacity.
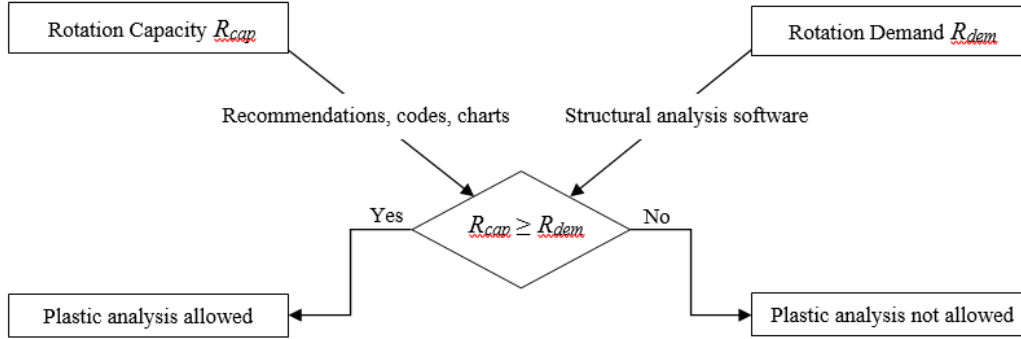

Figure 1 – Criterion to allow for plastic analysis

Ductility is defined as the capacity to undergo large deformations beyond first yield without significant reduction in ultimate strength. With respect to sections or members acted by bending moments, the rotation capacity R_{cap} is a means to quantify a section's ductility, and is usually defined as in Eq. (1), where θ_{pl2} is the limiting rotation at which the sustained bending moment drops below M_{pl}.

$$R_{cap} = \frac{\theta_{pl2} - \theta_{pl}}{\theta_{pl}} = \frac{\theta_{pl2}}{\theta_{pl}} - 1 \tag{1}$$

Figure 2 – Generalized moment-rotation curve and definition of rotation capacity R_{cap}

Several studies have been performed throughout the years to determine practical maximum plastic rotation requirements. Since the required rotation (or rotation demand R_{dem}) differs with the loading and geometry of the considered structure and because the calculation of R_{dem} for complex structures can sometimes be complicated, time consuming and unreliable ([1], [2]), a fixed value of R_{dem} is usually prescribed as a minimum plastic rotation requirement in practical design.

Several such R_{dem} values can be traced back in the relevant literature. In a non-exhaustive manner, one can refer to the Eurocode 3 Editorial Group ([3]), suggesting that a value $R_{dem} = 3$ was suitable for plastic design, while Korol and Hudoba ([4]) recommend a value of $R_{dem} = 4$. Hasan and Hancock ([5]) and Zhao and Hancock ([6]) used a limitation of $R_{dem} = 4$ to determine suitable plastic slenderness for the Australian Standard AS 4100 ([7]). Kuhlmann ([8]) and Neal ([9]) suggested that a value of $R_{dem} = 2$ was sufficient for continuous beams. Stranghöner, Sedlacek and Boeraeve ([10]) investigated the behavior of hollow sections and outlined that different rotation requirements are necessary than for I-sections, and they found that $R_{dem} = 3$ was adequate for continuous beams.

Rules allowing the use of plastic design are required for the design of structural steel members. Hence, plate slenderness limits have been established where sections are considered as being constituted of individual flat plate elements. In the Eurocode 3 and A.I.S.C. standards, a section

is classified as "class 1" or "compact" if it can reach a rotation capacity larger than 3. Only for such sections plastic analysis and design may be performed.

Although many papers and reports ([8], [10] to [16], …) have evidenced that the rotation capacity R_{cap} must be associated with the demand in rotation R_{dem} (see Fig. 1), it remains of common practice in most major standards (Eurocode 3 [17], A.I.S.C. [18], A.S. 4100 [7]) to allow designers to resort to a so-called "plastic analysis and design" on the sole (direct or indirect) determination of R_{cap}, irrespective of R_{dem}. Further, codes typically suggest individual b/t ratios of the various plates comprised within the section to be governing the cross-section overall response, regardless of many parameters such as moment distribution (gradient), level of shear, ultimate-to-yield stress ratio, height-to-length ratio, ductility reserves, … In addition, sections' plate constituents are kept being considered under ideal support conditions – i.e. webs and flanges are assumed as pinned-pinned, while flanges half widths are considered pinned-free. Although several studies have shown that this should be improved ([19], [20]) and that code-ready proposals begin to emerge ([21]), cross-section classification procedures as based on tables with b/t limit values are still in application.

Besides, a recently-developed alternative design approach, the Overall Interaction Concept (O.I.C., see [20]) proposes to use a generalized cross-section overall relative slenderness (see Eq. (2)), as one as one of its main features, that allows to account for actual plate's behavior and response, including element interaction.

$$\bar{\lambda}_{CS} = \sqrt{\frac{R_{RESIST}}{R_{STAB,CS}}} \qquad (2)$$

In Eq. (2), R_{RESIST} represent the factor by which a given initial loading has to be multiplied to reach the pure *resistance* limit, and $R_{STAB,CS}$ is the factor used to reach the local buckling load of the cross-section (*stability* limit). λ_{CS} therefore constitutes a measure of the cross-section – as a whole – sensitivity to local buckling as well as of overall compactness and ductility reserves. As for sections in simple bending, λ_{CS} may be seen as an alternative, more global, parameter referring to the cross-sectional rotation capacity.

The present paper describes a series of bending tests that aimed at characterizing experimentally the relationship between ductility (R_{cap}) and cross-section compactness (λ_{CS}). Besides, numerical F.E. models created in the purpose of being substituted to physical tests are described, and tested against the experimental results.

2. Experimental test series on hollow sections beams

2.1. Objectives and test program

A test program undertaken at the University of Applied Science of Western Switzerland – Fribourg consisted in bending tests on hollow structural shapes (either Rectangular Hollow Sections R.H.S. or Square Hollow sections S.H.S.), of various dimensions and with different support and loading arrangements. They mainly aimed at (i) providing experimental references on the inelastic behavior and response of such members – and especially with respect to ultimate load carrying capacity and available rotation capacity –, and at (ii) calibrating and validating F.E. numerical models that shall later be used extensively in parametric studies. Specimens were selected so as to lie close to the so-called class 1-2 border, i.e. the limit beyond which plastic

analysis shall not be allowed because at least one plate in the cross-section possesses a too high b/t ratio, given its distribution of stresses.

Table 1 – Test program summary

Test specimen	h_{meas} [mm]	b_{meas} [mm]	t_{meas} [mm]	L [mm]	f_y [N/mm²]	f_u [N/mm²]	E [kN/mm²]	Test configuration
RHS_150*100*8_SS_3P	149.60	99.94	8.35	2600	391	554	205.7	
RHS_180*80*4.5_SS_3P	179.35	78.52	4.80	2600	389	539	198.5	
RHS_150*100*5_SS_3P	148.97	99.17	5.26	2600	420	573	211.2	Simply supported
RHS_220*120*6.3_SS_3P	217.55	120.75	6.40	2600	396	536	211.1	3-point bending
SHS_180*6.3_SS_3P	179.59	179.59	6.58	2600	393	524	206.9	
SHS_180*8_SS_3P	179.44	179.44	7.89	2600	384	532	208.0	
RHS_150*100*8_SS_4P	149.48	99.86	8.16	2600	391	554	205.7	
RHS_180*80*4.5_SS_4P	179.59	79.71	4.81	2600	389	539	198.5	
RHS_150*100*5_SS_4P	149.13	99.48	5.13	2600	420	573	211.2	Simply supported
RHS_220*120*6.3_SS_4P	219.40	120.86	6.42	2600	396	536	211.1	4-point bending
SHS_180*6.3_SS_4P	179.68	179.68	6.68	2600	393	524	206.9	
SHS_180*8_SS_4P	179.39	179.39	7.91	2600	384	532	208.0	
RHS_180*80*4.5_PR_C	179.19	79.06	4.76	4800	385	527	207.9	
RHS_150*100*5_PR_C	148.78	99.49	5.20	4800	404	547	213.1	
RHS_220*120*6.3_PR_C	219.10	120.45	6.51	4800	393	532	202.4	Propped-cantilever centrally loaded
SHS_180*6.3_PR_C	179.57	179.57	6.72	4800	391	532	206.8	
SHS_180*8_PR_C	179.30	179.30	7.94	4800	385	530	213.4	
RHS_180*80*4.5_PR_O	178.96	79.45	4.63	4800	387	537	205.4	
RHS_220*120*6.3_PR_O	219.03	120.66	6.51	4800	394	533	210.3	Propped-cantilever off-centrally loaded
SHS_180*6.3_PR_O	179.55	179.55	6.53	4800	386	529	207.7	

Four different test setup configurations were used: 3-point and 4-point bending static systems with a span length of 2.6 m (see § 2.3), as well as propped-cantilever configurations with mid-span and outer loaded point loads with a span length of 4.8 m (§ 2.4).
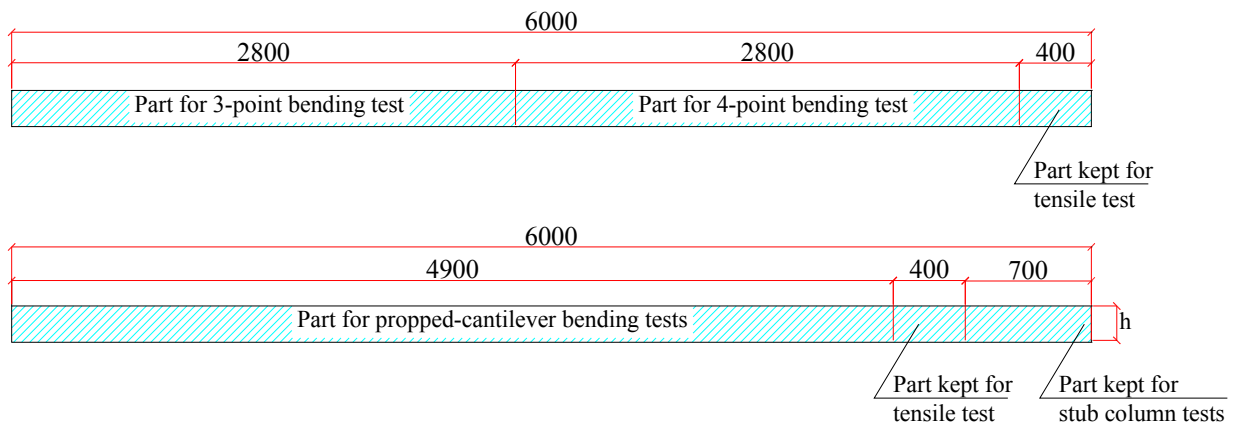

Figure 3 – Use of 6.0 m samples

Six different cross-sections were considered, all corresponding to class 1 or "end of class 1" sections according to Eurocode 3 classification. Their dimensions were chosen so as to have different relative cross-sectional slenderness values λ_{CS} ranging from 0.2 to 0.56. Tested beams were fabricated using a hot-formed process with S355steel grade.

The 6.0 m profiles were cut as follows: for the simple supported configuration, two 2.8 m specimens were cut and a 400 mm sample was kept for tensile tests. For the propped-cantilever configurations, a 4.9 m segment was kept for being tested in bending, while a 400 mm part served for tensile tests and a 700 mm piece was kept for a stub column test. The specimens' lengths were chosen high enough so that the failure mode would occur predominately in bending with little influence of shear. Table 1 summarizes the test program and reports on the measured geometric dimensions of all tested profiles and their main material properties: Young's modulus E, tensile yield strength f_y and ultimate yield strength f_u – the material values reported in Table 1 are average values from four coupon specimens cut from each section considered.

2.2. Tensile coupon and stub columns tests

Hot-formed structural steel profiles are assumed to usually exhibit uniform material properties within the entire cross-section, owing to their fabrication process. Their stress-strain relationship typically displays a sharply defined yield point, and a yield plateau followed by strain hardening behavior. For each of the tested tubular specimens, four tensile coupons were extracted from each flat face. The coupons were 270 mm in length and tested under a constant strain rate of 2.5 mm/min. Some of the tested coupons are shown in Fig. 4a, and Fig. 4b plots typical stress strain responses of the tested coupon, where usual carbon steel characteristics can be observed, namely the presence of plastic plateaus.
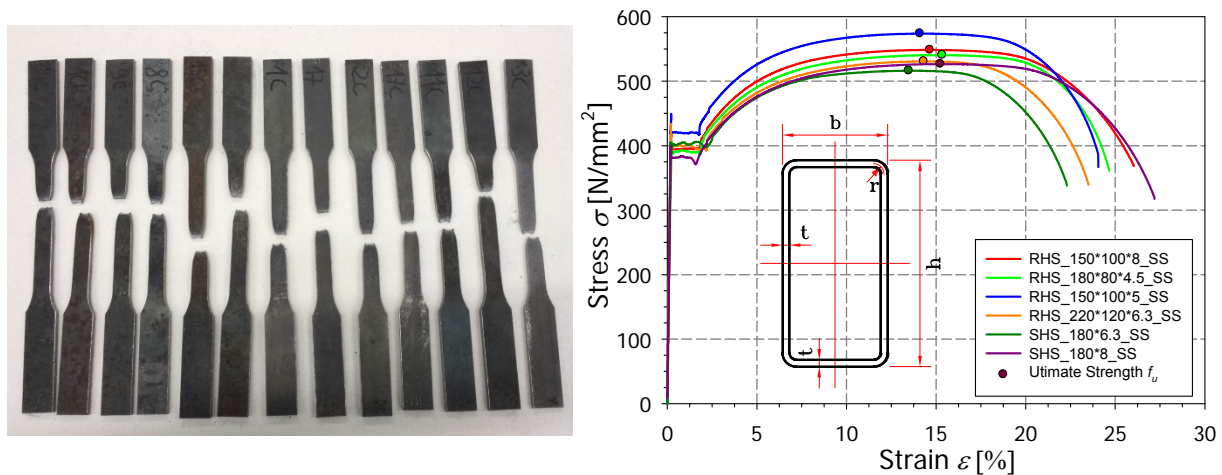

Figure 4 – a) Samples after tensile test – b) Stress-strain curves for RHS and SHS coupons

Besides tensile tests, seven stub column tests were performed so as to characterize the behavior of the various sections considered under compression. The stub columns lengths were chosen as being three times the height of the cross-section to limit flexural buckling. Each member length, dimensions and weight were measured prior to testing and were used for the calculation of the measured areas assuming a density of 7850 kg/m^3. The end sections of each stub were carefully manufactured, namely regarding flatness and perpendicularity to the acting compression force. Two strain gauges have been attached at mid-height of each specimen, on adjacent plates. The

5

testing machine was a 5000 kN hydraulic rig controlled through displacement increments. Two milled flat plates 250×250×150 made of high strength steel ($f_y = 2200$ N/mm^2) were placed on each side of the stub column in order to protect the testing machine surface. Four LVDTs were positioned near the stub ends to record the average end-shortening behavior. The strains gauges indicated if the compression was being applied evenly and characterized accurately the load-displacement response of the specimen in the elastic range. Failure shapes of stub columns are shown in Fig. 5b.

Figure 5 – Testing and failure shapes of stub columns

Cross-sections were classified according to Eurocode 3 ([17]), for bending and compression cases (Table 2). On the basis of nominal geometrical dimensions and estimated yield strengths, all sections, in bending, are seen to be plastic (class 1 sections); however, cross-sectional classes range from plastic to slender in compression (class 1 to class 4). Plate relative slenderness λ_p values reported in Table 2 (see Eq. (3)) correspond to the maximum relative slenderness value λ_p of the cross-section constituent plates, where k is the buckling coefficient and Poisson's ratio $\nu = 0.3$; the correction factor $\varepsilon = \sqrt{(235 / f_y)}$ to account for non S235 steel grades was also considered. In contrast to λ_{CS}, the more common parameter λ_p is relative to the weakest plate within the section, and does not account for interactions between plates (i.e. ideal support conditions for plates are considered).

$$\lambda_p = \sqrt{\frac{f_y}{k \cdot \frac{\pi^2 \cdot E}{12 \cdot \left(1 - \nu^2\right)} \cdot \left(\frac{t}{b}\right)^2}} \tag{2}$$

Table 3 summarizes the stub column test results for all seven specimens. All sections exhibited a plastic response, at least to some extent; detailed analysis of load-displacement records indeed showed a certain reserve of ductility, even though some specimens did not reach their full plastic capacity. Accordingly and from the classifications in bending according to Table 2, some sections were expected to possess a high rotation capacity in bending while others shall have a more limited one.

Table 2 – Cross-section classification

Name of specimen	h	b	t	r	f_y	$\dfrac{(h-t-2r)/t}{\varepsilon}$	$\dfrac{(b-t-2r)/t}{\varepsilon}$	λ_p compression	λ_p bending	Class in compression	Class in bending
	[mm]	[mm]	[mm]	[mm]	[N/mm²]	[-]	[-]	[-]	[-]		
RHS_150×100×8	150	100	8.0	12.00	400	19.2	11.1	0.34	0.20	1	1
RHS_180×80×4.5	180	80	4.5	6.75	400	47.0	18.0	0.83	0.34	4	1
RHS_150×100×5	150	100	5.0	7.50	420	34.8	21.4	0.61	0.38	2	1
RHS_220×120×6.3	220	120	6.3	9.45	400	40.3	19.6	0.71	0.35	3	1
SHS_180×6.3	180	180	6.3	9.45	400	32.1	32.1	0.56	0.56	1	1
SHS_180×8	180	180	8.0	12.00	400	24.1	24.1	0.42	0.42	1	1

For the RHS_180*80*4.5_PR_O, SHS_180*6.3_PR_C, RHS_220*120*6.3_PR_C sections, local buckling was seen to develop unevenly on one side owing to a slightly imperfect flatness on the end sections which resulted in an unexpected bending moment introduction on the specimen, however of relatively small magnitude and influence. Experimental defaults as well as other experimental uncertainties may explain why some class 1 or 2 tests have reached ultimate loads slightly below the plastic load.

Table 3 – Measured properties and ultimate loads of stub column tests

Test specimen	Length	Weight	Area	N_{pl}	N_{exp}	N_{exp} / N_{pl}
	[mm]	[kg]	[mm²]	[kN]	[kN]	[-]
RHS_150*100*8_PR_C	450.5	12.85	3633.6	1440.6	1697.5	1.18
RHS_180*80*4.5_PR_C	541.0	9.50	2237.0	861.6	822.7	0.95
RHS_180*80*4.5_PR_O*	540.5	9.40	2215.5	856.5	805.6	0.94
RHS_150*100*5_PR_C	541.0	8.35	2358.5	952.6	943.4	0.99
SHS_220*120*6.3_PR_C*	663.0	21.25	4083.0	1604.5	1577.5	0.98
SHS_220*120*6.3_PR_O	662.0	21.35	4108.4	1617.0	1613.7	1.00
SHS_180*6.3_PR_C*	540.0	19.05	4494.0	1756.7	1749.8	1.00

*Buckling occurred slightly unevenly due to accidental (of negligible influence) moment introduction

2.3. 3-point and 4-point bending tests

Some six beams were tested in typical 3-point bending configurations (Figs. 6 and 7). The experimental support arrangement consisted in a 30 *mm* diameter roller, mounted on a steel plate attached to the extremities. Loading was applied by means of two hydraulic jacks acting on two threaded bars connected to a stiff loading beam (cf. Fig. 6). Loading was introduced in the specimen with half-round loading points and through a 40 *mm* thick and 50 *mm* wide plate to avoid high levels of stress concentration. Various transducers were used to monitor the beam's response:

- Load cells were located under each support and under the jacks to record the support reactions and the loading force, respectively;

- Inclinometers were fixed at both ends of the beam to measure the beam end rotations;

- Linear variable displacement transducers (LVDTs) were positioned along the beam to record the beam deflection;

- Strain gauges were fixed on the tension flange to measure both deformation and curvature.

Loading was carried out under displacement control and all readings were taken using an electronic data acquisition system at a 2 *Hz* pace. Fig. 7 displays the deformed shape of specimen RHS_150*100*5_SS_3P during testing.

All six beams were tested up to and beyond failure. In most cases, local buckling occurred before beams reached their plastic moment M_{pl} except for the case of specimen RHS_150*100*8 for which large deflections were reached and the test had to be aborted before unloading due to excessive deformations and experimental limitations.
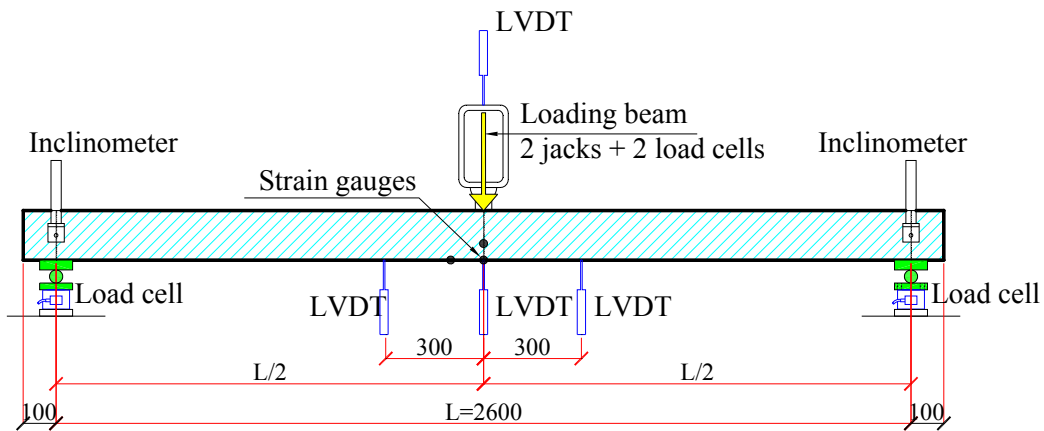
Figure 6 – Position of the LVDTs on the 3-point bending beam (dimensions in *mm*)
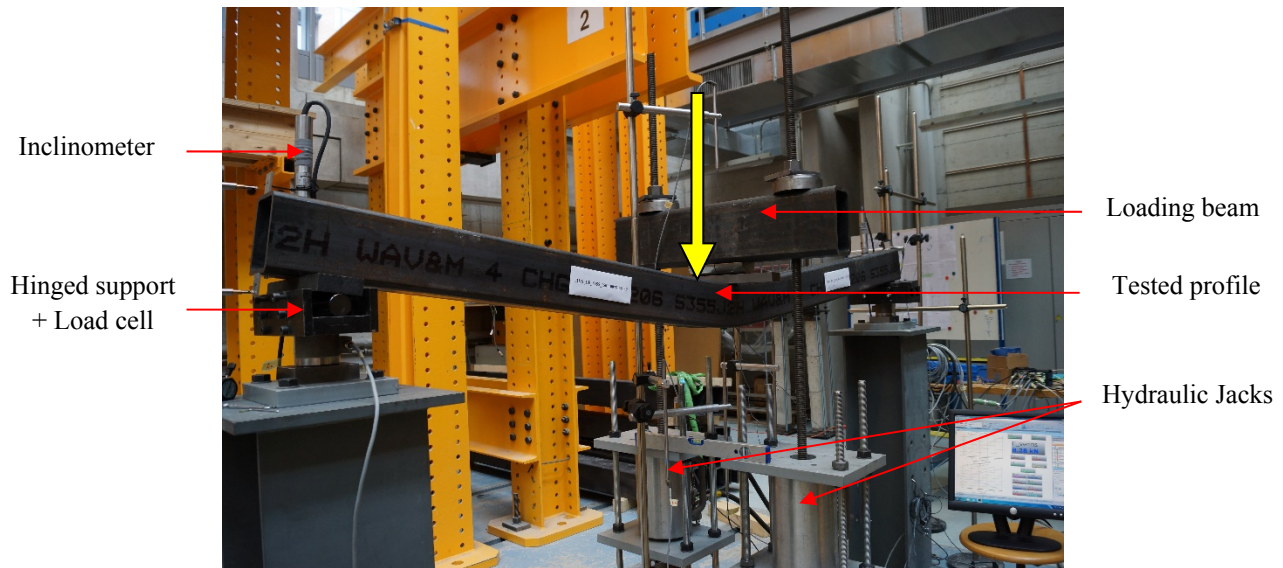
Figure 7 – Deformed shape of RHS_150×100×5_SS_3P specimen

The maximum shear ratio V / V_{pl} for all 3-point bending configurations was never higher than 32%, so no significant influence of shear on the resistance to bending shall be accounted for.

The onsets of local buckling were typically quite localized due to the loading introduction that induced high level of stress concentrations. Hence, even with the loading applied through a 40 *mm* thick plate, loading at high deformations began to be non-uniformly distributed on the

area of the plate but was rather effective on the plate extremities in contact with the corners edges. This can explain why beams failed prematurely by reaching 98% of the plastic moment M_{pl} – while being all class 1 in bending – and with an ultimate deflection of 33 mm. The RHS_150*100*8_SS_3P specimen – characterized by a very stocky section $\lambda_{p,bending} = 0.2$ – was less affected by load introduction effects, and reached a quite large 139 mm deflection at peak load.
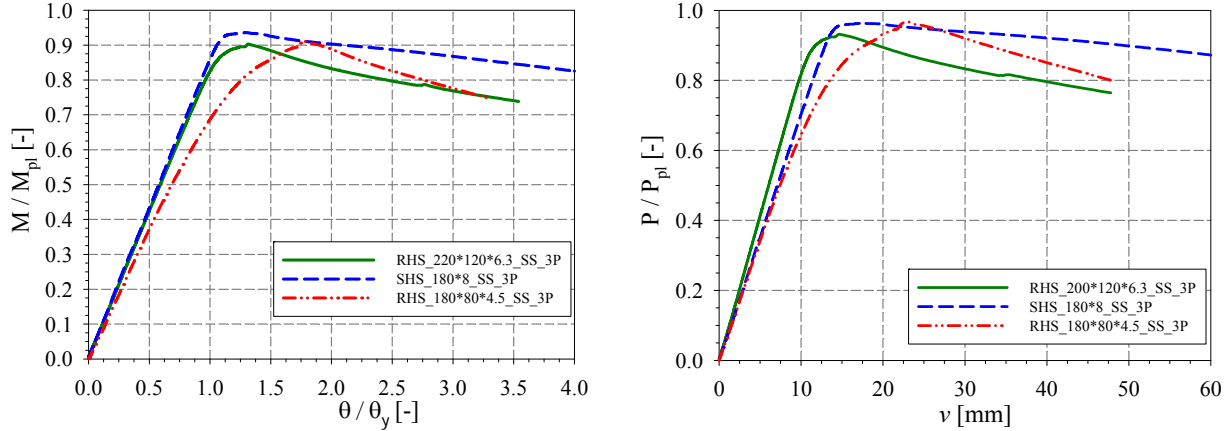

Figure 8 – a) Normalized moment-rotation curves – b) Normalized load-deflection curves

Fig. 8a presents relative moment-rotation curve of three beams for which M_{pl} is the plastic moment calculated from measured cross-sections properties, and θ_y is the yield rotation at the beams' ends – θ_y is calculated for the middle cross-section to first reach the elastic moment. Fig. 8b represents the total load vs. deflection response, where P_{pl} is the theoretical plastic collapse load of the system and v is the deflection of the beam at mid-span. According to the plotted curves, it appears clear that all beams failed prior to reaching their plastic capacity, however by a small amount.

Table 4 – Experimental collapse loads for 3-point bending tests

Name of specimen	$M_{pl,fy}$	$P_{pl,fy}$	θ_y	M_{ult}	M_{ult}/M_{pl}	P_{ult}	P_{ult}/P_{pl}	θ_u/θ_y	v_u	$\lambda_{p,bending}$
	[kNm]	[kN]	[°]	[kNm]	[-]	[-]	[-]	[-]	[mm]	[-]
RHS_150×100×8_SS_3P	69.8	107.4	0.95	84.6	1.21	134.8	1.26	7.53	138.9	0.20
RHS_180×80×4.5_SS_3P	50.5	77.6	0.81	46.3	0.92	75.3	0.97	1.59	22.9	0.34
RHS_150×100×5_SS_3P	50.5	77.6	0.99	46.6	0.92	76.7	0.99	1.94	33.4	0.38
RHS_220×120×6.3_SS_3P*	113.8	175.1	0.64	98.7	0.87	156.4	0.89	1.28	13.8	0.35
RHS_220×120×6.3_SS_3P	113.4	174.4	0.64	101.6	0.90	161.3	0.92	1.34	14.6	0.35
SHS_180×6.3_SS_3P	112.3	172.8	0.79	105.6	0.94	166.6	0.96	1.31	17.6	0.56
SHS_180×8_SS_3P	128.4	197.5	0.77	121.1	0.94	191.8	0.97	1.32	17.3	0.42

* Rectangular cross-section 220x120x6.3 had two test specimens for the simply supported 3-point bending

Besides the 3-point configurations, six beams were tested under 4-point loading arrangements (cf. Fig. 9), so as to characterize the effect of moment gradient; Fig. 10 shows SHS_180*6_SS_4P specimen at failure. The 4-point bending test setups differed from the 3-point bending arrangement only in the insertion of a spreader beam over the tested specimen in order to apply equal loads on both loading points located at quarter lengths of the hinged

supports. The low shear ratios V / V_{pl} for all 4-point bending configurations were similar to the 3-point bending ones, except for the central segments of the specimens which were free from shear forces; consequently, the influence of shear was disregarded here as well. LVDTs and strain gauges were placed under the loading points and at mid-span to record the beam response accurately as shown in Fig. 9. Load cells were placed under both supports and under hydraulic jacks; inclinometers were positioned at the beams' ends (Fig. 9).
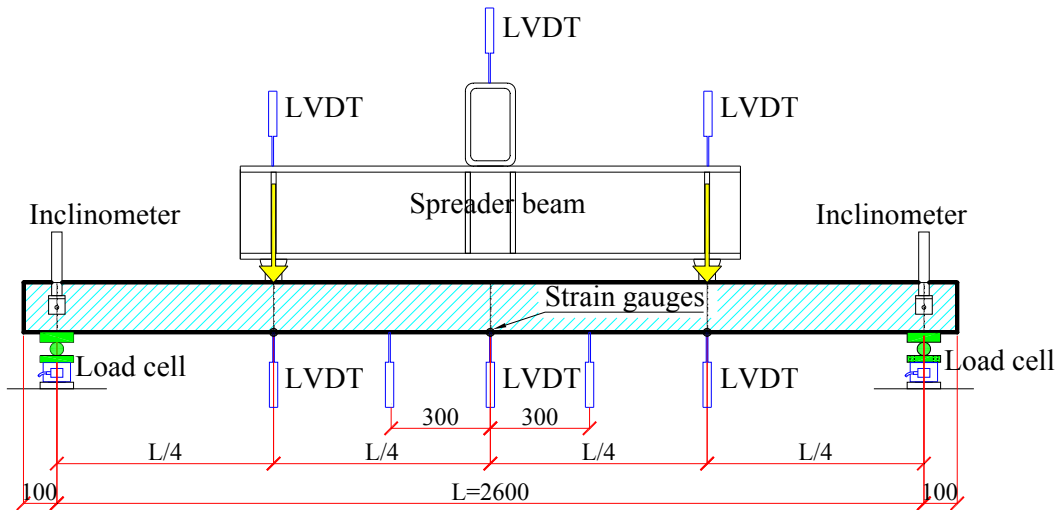
Figure 9 – Test setup of the 4-point bending beam
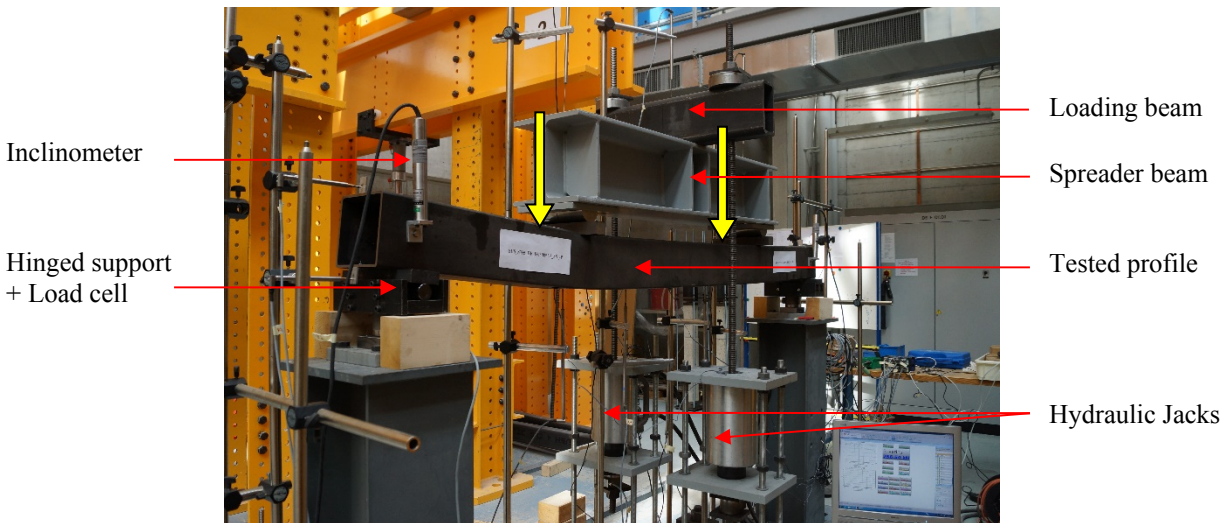
Figure 10 – Deformed shape of a 4-point bending beam

During testing, the beams' deflections remained symmetric until peak loads were reached, and the specimens kept a symmetrical deformed pattern beyond peak for most of the tests. In a few cases however, local buckling failure modes started developing at either the right or left loading point as shown in Fig. 11b for RHS_180*80*4.5, causing unsymmetrical deflected shapes. The onset of local buckling was localized under the load application (either on the left or right loading point) owing to a high level of stress concentration. Fig. 11aa represents non-dimensional moment vs. beam end rotations; the difference between the two curves at points of

load application highlights the occurrence of local buckling and the beam's unsymmetrical response.
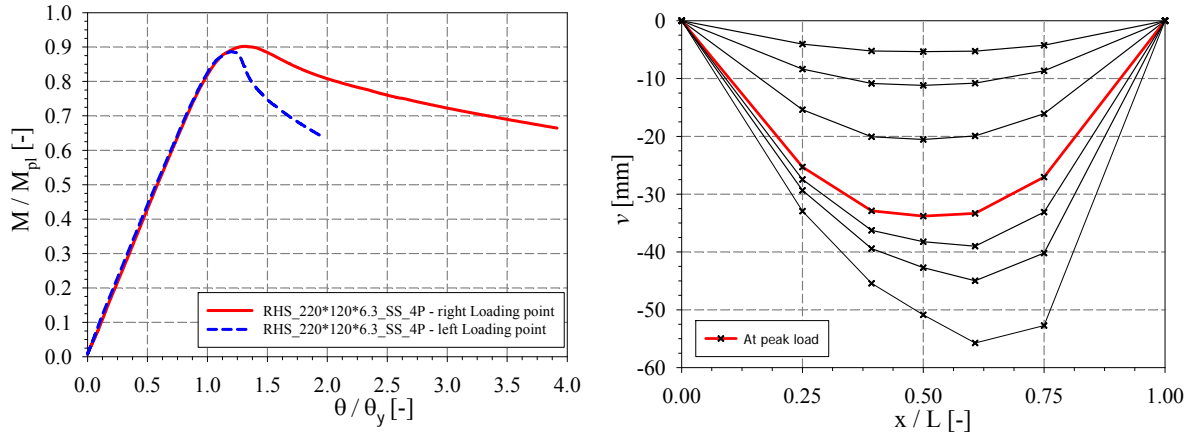

Figure 11 – a) Moment-rotation curve of RHS_220×120×6.3 – b) Relative deflected shape of RHS_180×80×4.5

The ultimate bending moment and the peak load did nicely match the plastic capacity in all tests except for the RHS_150*100*8 specimen who attained strain hardening but loading had to stopped before reaching the peak load owing to excessive vertical deformations; the beam deflected rather elastically and without the occurrence of local buckling until reaching a vertical displacement of 150 *mm* – that corresponds to the maximum hydraulic jack capacity – without attaining the system peak load.

Table 5 summarizes the experimental results for all tested specimens. Yield rotation θ_y is calculated from the middle segment first reaching the elastic bending moment, while system plastic collapse loads P_{pl} are computed for beams attaining their plastic capacities.

Table 5 – Experimental collapse loads for 4-point bending tests

Name of specimen	$M_{pl,fy}$	$P_{pl,fy}$	θ_y	M_{ult}	M_{ult} / M_{pl}	P_{ult}	P_{ult} / P_{pl}	$\theta_{u,a}$ / θ_y	$\theta_{u,b}$ / θ_y	$v_{u,a}$	$v_{u,b}$
	[kNm]	[kN]	[°]	[kNm]	[-]	[-]	[-]	[-]	[-]	[mm]	[mm]
RHS_150×100×8_SS_3P**	68.4	105.3	1.42	83.2	1.22	131.3	1.25	9.41	8.88	149.2	142.0
RHS_180×80×4.5_SS_3P	51.0	78.5	1.22	47.3	0.93	75.0	0.95	1.93	2.04	25.3	27.0
RHS_150×100×5_SS_3P	49.5	76.1	1.49	47.9	0.97	77.0	1.01	2.94	2.64	47.3	43.0
RHS_220×120×6.3_SS_3P	115.3	177.4	0.96	103.3	0.90	163.4	0.92	1.23	1.34	12.9	14.1
SHS_180×6.3_SS_3P	113.8	175.1	1.18	103.7	0.91	164.8	0.94	1.35	1.26	16.7	17.0
SHS_180×8_SS_3P	128.6	197.8	1.15	125.3	0.97	181.9	0.92	1.63	1.50	20.6	19.6

** Specimen did not reach failure – test was stopped due to excessive vertical deformations

2.4. Propped-cantilever bending tests

In order to complement 3-point and 4-point bending tests on *statically determinate* beams, a series of tests on *statically indeterminate* beams was performed, with so-called propped-cantilever arrangements with either central or offset point loads.

Five propped-cantilever specimens of 4.8 *m* span length were tested with the loading being applied at mid-span. Specimens have been fixed to a braced support by welding a 30 *mm* thick plate to the beam's end and then bolting it with eight 10.9 M24 bolts. All end plates were chosen

11

to be thick enough so as to be considered as perfectly rigid and full penetration welds were realized.

In an attempt to monitor the specimens' strains and curvature at hinges' locations with limited interference of local buckling on readings, strain gauges were fixed on the tension flanges of critical sections. The fixed support strain gauge was placed 50 *mm* away from the end plate due to the presence of the weld and another gauge was placed at mid-span. The inclinometer was attached to the hinged end to measure the beam end rotation and a load cell was placed under the hinged support to measure the support reaction. Loading was introduced in the same way as for the simply supported beams and two load cells were placed under the jacks to record the applied force. LVDTs were placed at mid-span and at quarter span length to measure the beams deflection. The test setup is shown in Figs. 12 and 13.
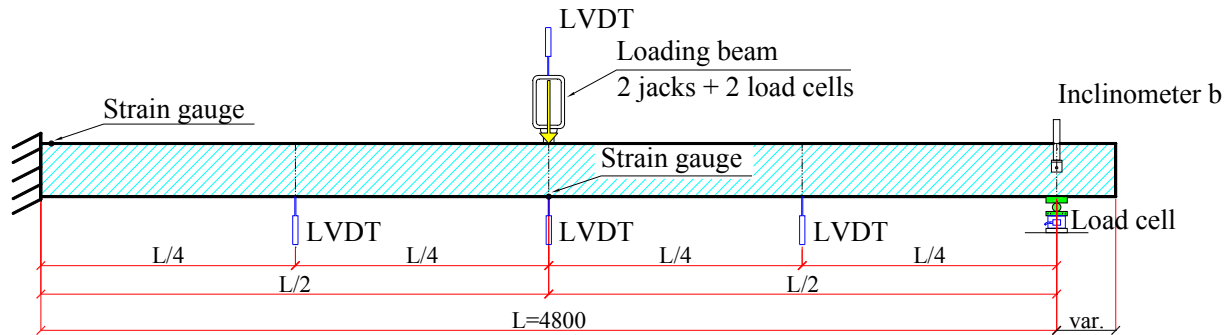

Figure 12 – Test setup of the propped-cantilever centrally loaded

Figure 13 – a) Deformed shape of a propped-cantilever centrally loaded – b) Connection detail on braced support

Plastic bending moments were first reached at the fixed support where plastic hinges developed; additional bending moment was then redistributed in span until the plastic moment and the peak load were attained, a plastic collapse mechanism being reached.

θ_y was calculated when the fixed-end section first reached the elastic moment. System collapse loads were calculated based on virtual work analyses and collapse mechanisms with classical assumption of rigid-plastic material behavior and plastic hinges of zero length, together with assumed elastic bending moment distributions after first hinges developed. Non-dimensional

moment-rotation curves could then be plotted using the rotation given by the inclinometer at the hinged end. Results are shown for SHS_180*80*4.5 specimen in Fig. 14; as expected, it is shown that, as the test progressed, fixed end moments grew higher than at mid-span. System peak loads were reached with premature local buckling at mid-span (i.e. before reaching the plastic moment in span).
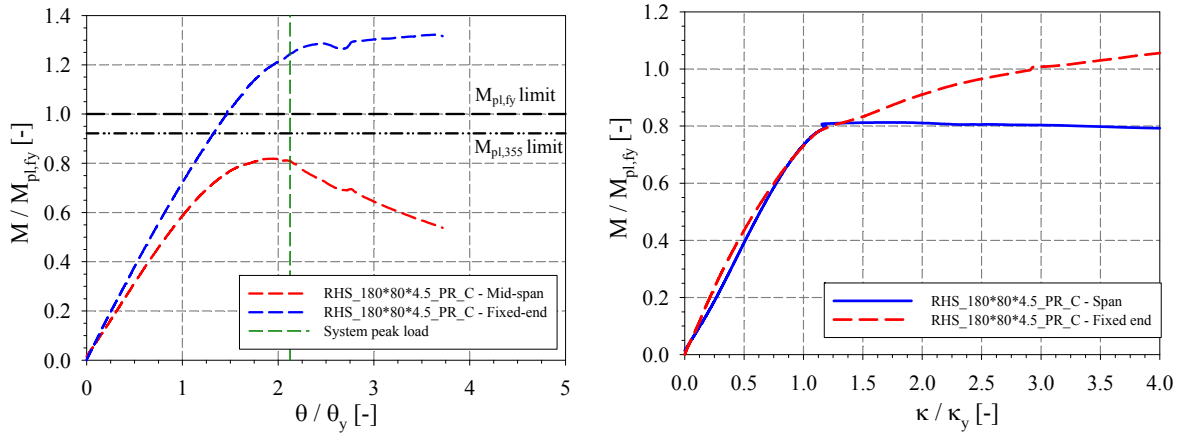

Figure 14 – a) Normalized moment-rotation of RHS_180×80×4.5 – b) Moment-curvature of RHS_180×80×4.5

Fig. 14b displays an example of normalized moment-curvature, for which the yield curvature $\kappa_y = M_{el} / EI$ is calculated from measured dimensions and material properties. In the elastic phase, a linear region with the same elastic flexural stiffness EI_y for both the fixed-end and mid-span cross-sections is observed, followed by a gradual reduction in stiffness for the fixed-end and a sudden loss of stiffness at mid-span. Table 6 summarizes normalized span moments and fixed-end moment along with the system peak load for all tested specimens.

Table 6 – Experimental collapse loads for centrally loaded propped-cantilever

Name of specimen	$M_{pl,fy}$	$P_{pl,fy}$	θ_y	P_{ult}	P_{ult} / P_{pl}	$M_{ult,span}$	$M_{ult,span} / M_{pl}$	$M_{ult,fixed-end}$	$M_{ult,fixed-end} / M_{pl}$	θ_u / θ_y	v_u
	[kNm]	[kN]	[°]	[kN]	[-]	[kNm]	[-]	[kNm]	[-]	[-]	[mm]
RHS_180×80×4.5_SS_3P	49.6	62.0	0.95	59.2	0.95	40.4	0.81	66.1	1.33	2.12	62.4
RHS_150×100×5_SS_3P	48.1	60.1	1.17	61.4	1.02	46.0	0.96	58.1	1.21	2.82	106.9
RHS_220×120×6.3_SS_3P	115.1	143.9	0.81	126.4	0.88	97.9	0.85	144.1	1.25	2.23	64.2
SHS_180×6.3_SS_3P	113.8	142.3	0.96	123.9	0.87	97.8	0.86	134.9	1.18	1.36	36.0
SHS_180×8_SS_3P	129.1	161.4	0.92	152.2	0.94	112.96	0.87	169.7	1.31	3.16	99.6

Three additional propped-cantilever specimens of 4.8 *m* length were tested with loading applied at one third length from the hinged support. This arrangement was performed so that – unlike the propped-cantilever centrally loaded – the plastic hinge would first form in span and then, due to moment redistribution, failure would occur by the fixed-end reaching the plastic collapse load. Arrangements for the fixed end, hinged end and loading introduction were set similarly to the centrally loaded cantilever.

As shown in Fig. 15a's moment-rotation plot, plastic moments were first reached in span. Failure was then attained by the fixed-end reaching its plastic collapse load. Before the system peak load

was reached, span moment was higher than the fixed-end moment after which the span moment decreased and the fixed-end moment increased to reach the plastic moment.
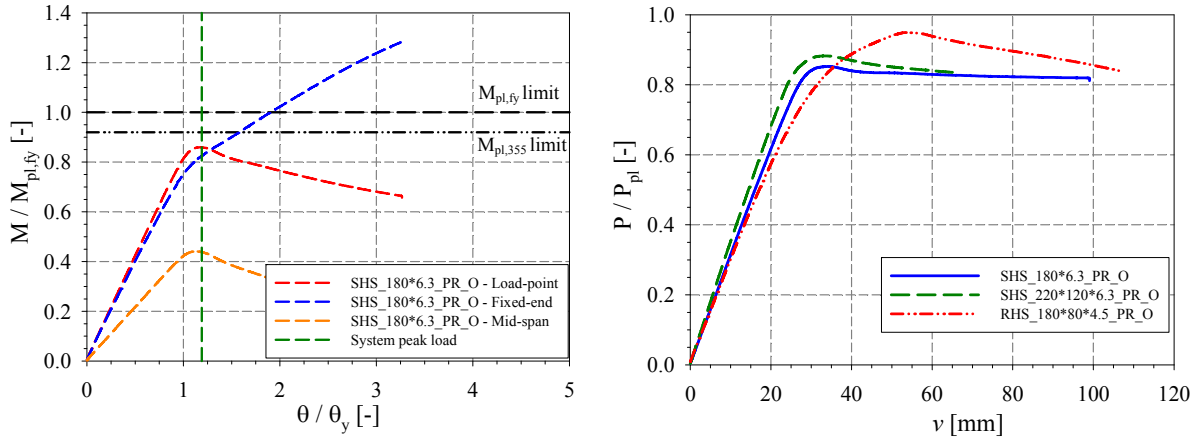

Figure 2 – a) Normalized moment-rotation of RHS_180×80×4.5 – b) Normalized total load-vertical mid-span displacement

System peak load occurred at variable vertical displacement levels ranging between 20 *mm* and 60 *mm*; the deflection of the three propped-cantilever off-centrally loaded are plotted against the normalized total load in Fig. 15b; deflection *v* was measured at the point of load application. Table 7 summarizes normalized span moments and fixed-end moment along with the system peak load and corresponding end rotation θ_u for the 3 specimens tested.

Table 7 – Experimental collapse loads for off-centrally loaded propped-cantilever

Name of specimen	$M_{pl,fy}$	$P_{pl,fy}$	θ_y	P_{ult}	P_{ult} / P_{pl}	$M_{ult,span}$	$M_{ult,span} / M_{pl}$	$M_{ult,fixed-end}$	$M_{ult,fixed-end} / M_{pl}$	θ_u / θ_y	v_u
	[kN.m]	[kN]	[°]	[kN]	[-]	[kN.m]	[-]	[kN.m]	[-]	[-]	[mm]
RHS_180×80×4.5_SS_3P	48.7	60.9	1.24	57.5	0.95	43.3	0.89	64.3	1.32	1.84	53.2
RHS_220×120×6.3_SS_3P	115.4	144.2	1.01	127.8	0.89	103.8	0.90	122.8	1.06	1.48	33.7
SHS_180×6.3_SS_3P	109.46	136.83	1.22	116.6	0.85	94.07	0.86	140.41	1.28	1.25	34.5

3. Development and validation of numerical models

Geometrically and materially non-linear shell F.E. numerical computations were performed by means of non-linear F.E.M. software FINELg, continuously developed at the University of Liège and Greisch Engineering Office since 1970 ([22]). The numerical models were developed to represent the specimens' properties and the test setup characteristics as closely as possible. Measured geometric dimensions were implemented and the section was modeled using 4 shell elements per corner to well represent the geometric static characteristics of the tested specimen. Averaged measured material stress-strain relationships were also included (Fig. 16a), through multi-linear material laws. Auto-equilibrated membrane residual stresses patterns were also implemented with a reference yield stress $f_y = 235$ *N/mm²* as shown in Fig. 16b.
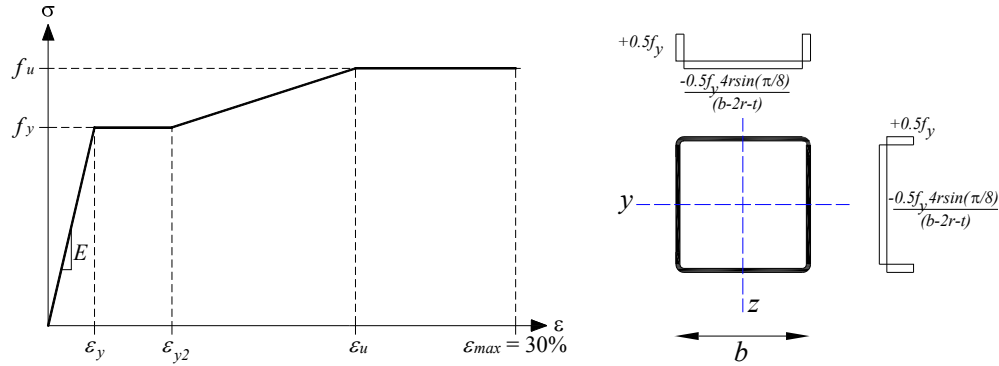
Figure 3 – a) Adopted material law for hot-formed sections; b) Auto-equilibrated residual stress pattern for Hot-finished tubular profiles - SHS and RHS

3.1. Modeling considerations

Special attention was paid to properly model the experimental support conditions. To accurately represent the actual hinged connection, only the bottom flange nodes were vertically supported at a distance of 100 *mm* away from the section end, as in the actual test; moreover, a rigid plate of 20 *mm* thickness was added under the hinged support (Fig. 17b).

Similar numerical models were developed for the propped-cantilever, and the end-plate connection deserved specific treatment since it could be shown to affect the behavior of the test. Same material law as for the main beam was adopted, and an increase in thickness for the first 10 *mm* of the beam was considered in order to account for the presence of the weld. Fixed horizontal support was applied at the compression part, as well as at the bolts' locations in the tension part (Fig. 17a).

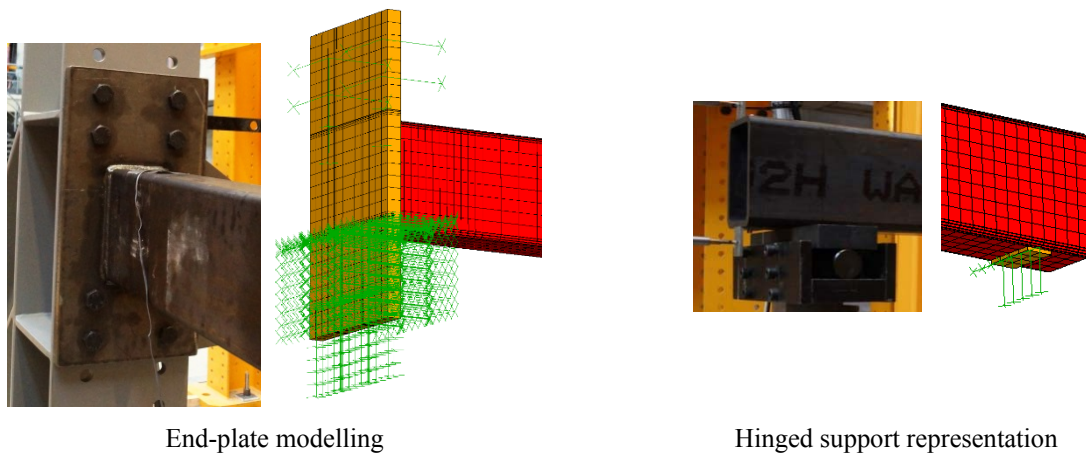End-plate modelling   Hinged support representation

Figure 4 – Details of supports modelling

Loading was introduced by means of 4 concentrated forces applied on the upper flange edges, and positioned at the 4 corners of the plate in contact with the tested beam, as was seen to be effective in the actual tests. Alternative load introduction modeling was also considered, in order to investigate their effect on the beams' responses and thus appropriate chosen modeling. Careful and detailed analyses and comparisons with test data allowed to show that Fig. 18 solution was the most appropriate modeling since it represented suitably the beams' responses in terms of moment-rotation diagrams.
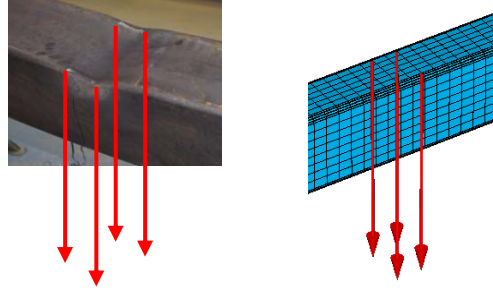
Figure 5 – Introduction of point loads in F.E. models

3.2. Influence of local geometrical imperfections

Distributions of initial geometrical imperfections are known to influence beams' responses in a non-negligible extent, especially *local* imperfections; in particular, post-peak behavior can be shown to vary greatly and significantly affect the rotation capacity R_{cap} ([19]). Since initial geometrical imperfections were not measured prior to testing, different sets of imperfection shapes and amplitudes were investigated numerically.

Basically, geometrical imperfections were introduced in two different ways. One is based on the deformation induced by the first eigenmode shape, to which a fixed amplitude is assigned. The second is introduced through an appropriate modification of node coordinates, where local geometrical imperfections are set for both webs and flanges with square half-wave shapes and with a chosen amplitude. In addition, a global default is introduced through a sinusoidal shape (similar to the member buckling shape), for both major and minor axes. Overall, some seven different geometrical imperfection patterns were tested (Imp 1 to Imp 7), as represented in Fig. 19.
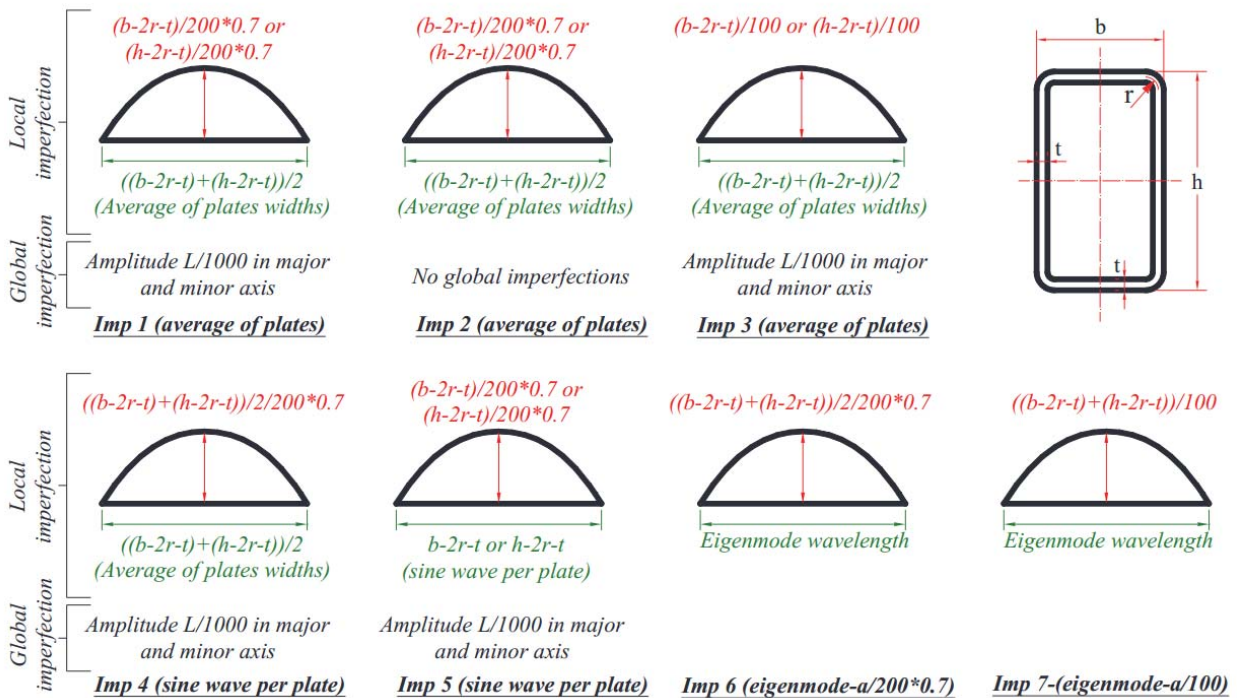

Figure 6 – Considered geometrical imperfections

The associated results were seen to vary in non-negligible extents, especially in terms of reported ductility (R_{cap} values), and to lie more or less closely to the experimental results. As displayed in Figs. 20 and 21, geometrical imperfections did not affect the elastic beam response, and no difference is visible between the various curves. Moreover, good accordance with the test result is observed which denotes adequate modeling in terms of support modeling, loading introduction, and suitable representation of the systems' stiffness. Nevertheless, the imperfections' shapes and amplitudes had a large influence on the the post peak response and therefore on the rotation capacity of the specimens (cf. definition of R_{cap} in Eq. (1)). Global geometrical imperfections had no influence on the beams tested in bending, since no difference between "Imp 1" and "Imp 2" moment rotation curves can be noticed. Global geometrical imperfections were nevertheless added to the local imperfections since they are present in a real specimen.
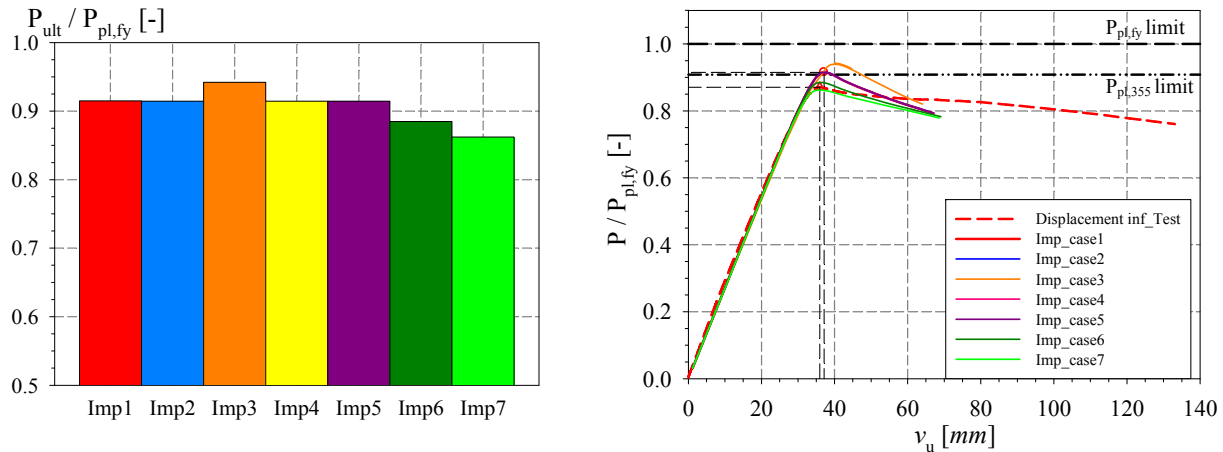

Figure 20 – Imperfections sensitivity for SHS_180×6.3_PR_C, a) comparison of the normalized ultimate load, b) load-displacement curves for the different imperfection patterns
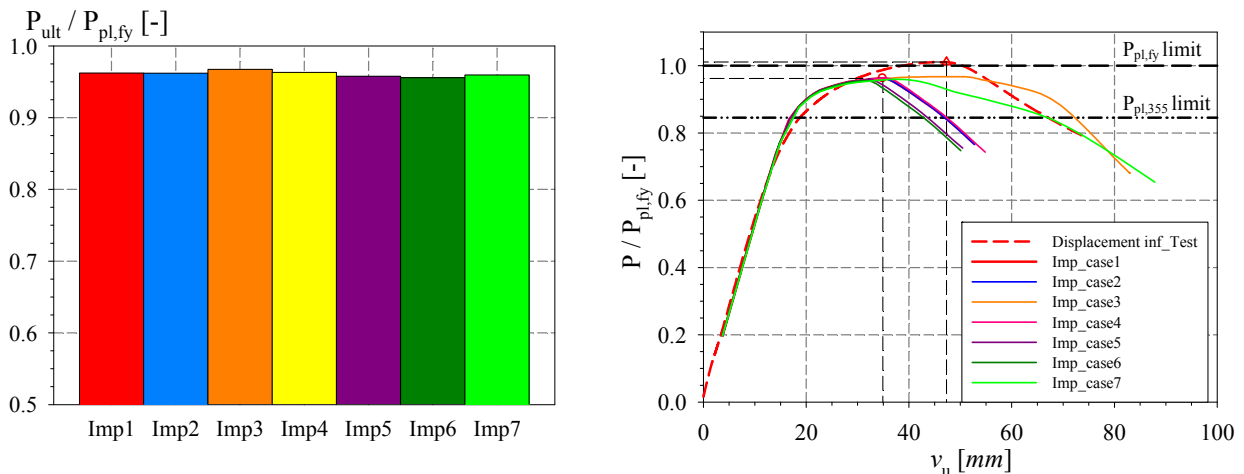

Figure 21 – Imperfections sensitivity for RHS_150×100×5_SS_4P, a) comparison of the normalized ultimate load, b) load-displacement curves for the different imperfection patterns

As a general trend, imperfections had an influence on the beam ultimate capacity as well as on its rotation capacity, as seen in Figs. 20 and 21. It shall also be noted that even though the

17

imperfection shape had an impact on the beam response, it is mainly their amplitude that lead to scatters in rotation capacities. Type 1 imperfection pattern was seen to lead to conservative results in term of rotation capacity, and was kept in the F.E. model validation studies.

4. Validation of test vs. numerical results

In the present section, experimental results are compared to the numerically predicted ones, based on actual cross-sectional dimensions, material properties and initial geometrical imperfection type 1.

4.1. Simply supported tests

Concerning the 3-point bending configurations, numerical simulations represented the real behavior quite accurately, especially in terms of elastic stiffness – Fig. 22 displays an example of numerical results nicely matching the experimental ones in the elastic part. Moreover, careful analysis of the F.E. results suggested that the introduction of loading shall be made responsible for sections slightly shying from reaching their plastic capacities, premature local buckling interacting with a certain level of crippling in key sections.
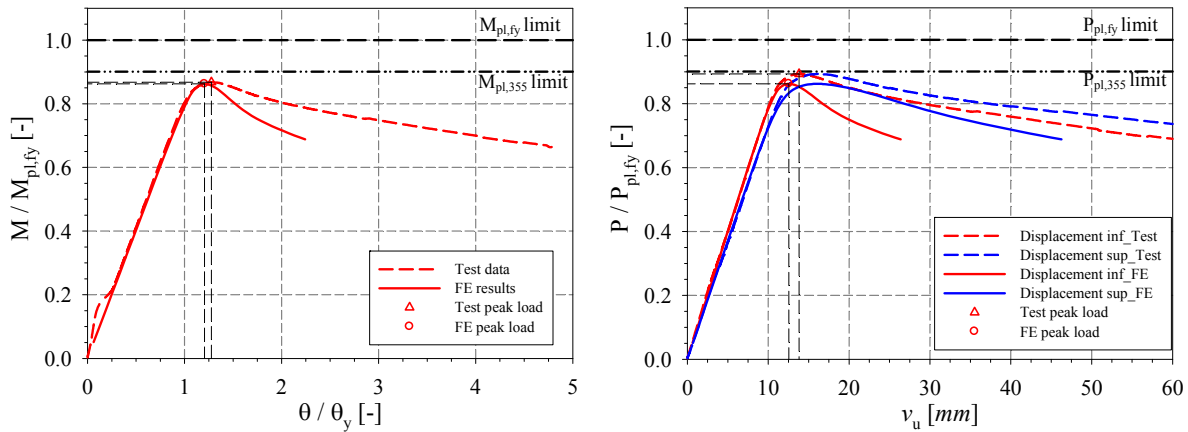

Figure 22 – RHS_220×120x6.3_SS_3P test vs. F.E. analysis comparison

Table 8 displays a comparison between F.E. and tests results in terms of bending moments and rotations at peak loads; on average, the deviation between numerical and experimental results in terms of peak moment was less than 2%. These results demonstrate the ability of the numerical model to well predict the capacity of sections. In terms of rotation at failure, the average deviation of numerical vs. experimental results was smaller than 20% with a deviation of 9%. These values represent a fairly good estimate of the rotation, since the large variability of the rotation capacity was previously identified and mainly attributed to the initial geometrical imperfections. We can also note that the numerical model always led to a safe underestimate for all the specimens in terms of the ultimate rotation.

Table 8 – Numerical vs. experimental results for 3-point bending tests

Test specimen	$P_{ult,FE}$ / P_{pl}	$P_{ult,exp}$ / $P_{ult,FE}$	$M_{ult,FE}$ / M_{pl}	$M_{ult,exp}$ / $M_{ult,FE}$	$\theta_{u,FE}$ / θ_y	$\theta_{u,exp}$ / $\theta_{u,FE}$
	[-]	[-]	[-]	[-]	[-]	[-]
RHS_150×100×8_SS_3P	1.16	1.08	1.16	1.04	6.15	1.22
RHS_180×80×4.5_SS_3P	0.93	1.04	0.93	0.98	1.37	1.16
RHS_150×100×5_SS_3P	0.98	1.00	0.98	0.94	1.46	1.33
RHS_220×120×6.3_SS_3P*	0.86	1.04	0.86	1.01	1.21	1.06
RHS_220×120×6.3_SS_3P	0.85	1.09	0.85	1.06	1.18	1.13
SHS_180×6.3_SS_3P	0.85	1.13	0.85	1.11	1.08	1.21
SHS_180×8_SS_3P	0.92	1.05	0.92	1.02	1.22	1.08
SHS_200×6_SS_3P	0.71	1.05	0.71	1.01	0.91	1.37

Similarly, for the 4-point loading configurations, a good accordance between numerical and experimental results was noticed, and Fig. 23 displays the particular case of specimen SHS_180x8_SS_4P, where similar conclusions to the 3-point bending case can be drawn. It can also be observed that the stiffness of the beam response is well represented in the elastic part. In the unloading phase, results slightly diverge between numerical and experimental results but similar trends are observed. A summary of results is reported in Table 9.
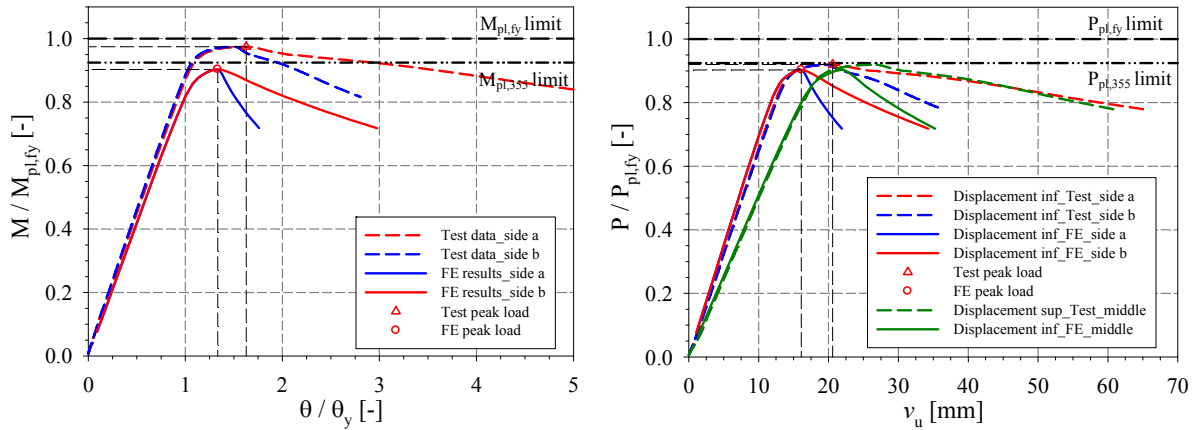

Figure 23 – SHS_180x8_SS_4P test vs. F.E. analysis comparison

Table 9 – Numerical vs. experimental results for 3-point bending tests

Test specimen	$P_{ult,FE}$ / P_{pl}	$P_{ult,exp}$ / $P_{ult,FE}$	$M_{ult,FE}$ / M_{pl}	$M_{ult,exp}$ / $M_{ult,FE}$	$\theta_{u,a}$ /θ_y	$\theta_{u,b}$ /θ_y	$\theta_{u,a,exp}$ / $\theta_{u,b,FE}$	$\theta_{u,a,exp}$ / $\theta_{u,b,FE}$
	[-]	[-]	[-]	[-]	[-]	[-]	[-]	[-]
RHS_150×100×8_SS_3P	1.11	1.12	1.11	1.09	13.13	12.85	0.72	0.69
RHS_180×80×4.5_SS_3P	0.91	1.05	0.91	1.02	1.60	1.60	1.20	1.27
RHS_150×100×5_SS_3P	0.96	1.05	0.96	1.01	2.18	2.18	1.35	1.21
RHS_220×120×6.3_SS_3P	0.85	1.09	0.85	1.06	1.28	1.29	0.96	1.04
SHS_180×6.3_SS_3P	0.84	1.12	0.84	1.08	1.08	1.06	1.24	1.19
SHS_180×8_SS_3P	0.90	1.02	0.90	1.08	1.33	1.34	1.22	1.12

A graphical plot that compares experimental and numerically-predicted peak moments for 3-point and 4-point bending configurations is presented in Fig. 24. It can be seen that all numerical simulations provide ultimate moments values in excellent accordance with the test results. All numerical predictions give values close to the ideal $M_{ult,exp}$ / $M_{ult,FE}$ = 1.0 line, while generally being safe-sided.
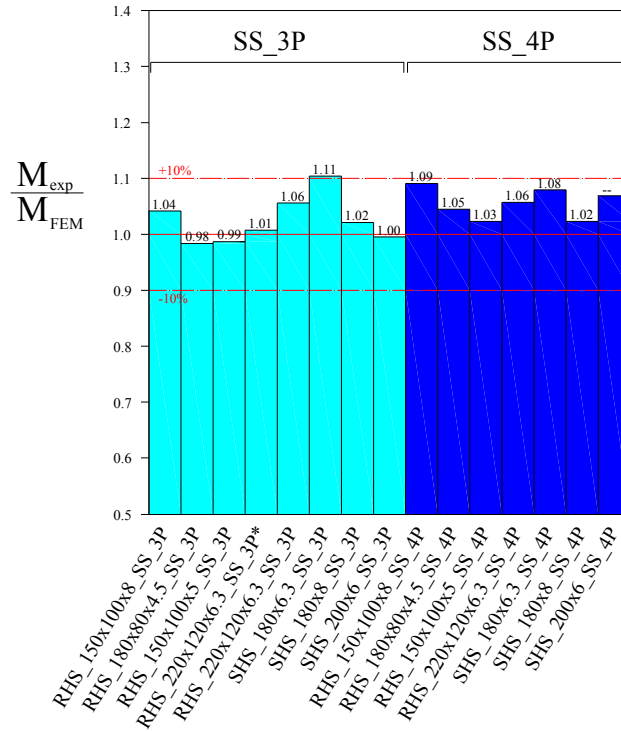

Figure 24 – Graphical comparison of ultimate moments for simply-supported configurations

4.2. Propped-cantilever tests

Specific end-plate modeling was used for the propped-cantilever configurations as well. Very good correspondence between experimental and numerical sources was generally observed – see example of test SHS_180×80×4.5_PR_C in Fig. 25. While system peak load and stiffness are nicely captured numerically, deflections at failure differ. This divergence is mostly attributed to the shape and amplitude of the initial geometrical imperfections adopted, as previously explained.

Moreover, while comparing moment-rotation curves in Fig. 25, a bigger divergence between moment in span and fixed-end moment can be noticed. These are associated with the experimental measurement capacities of the load cells, which could only record the vertical component of the reaction force at supports, while these reactions deviated from being only vertical at higher rotations level.
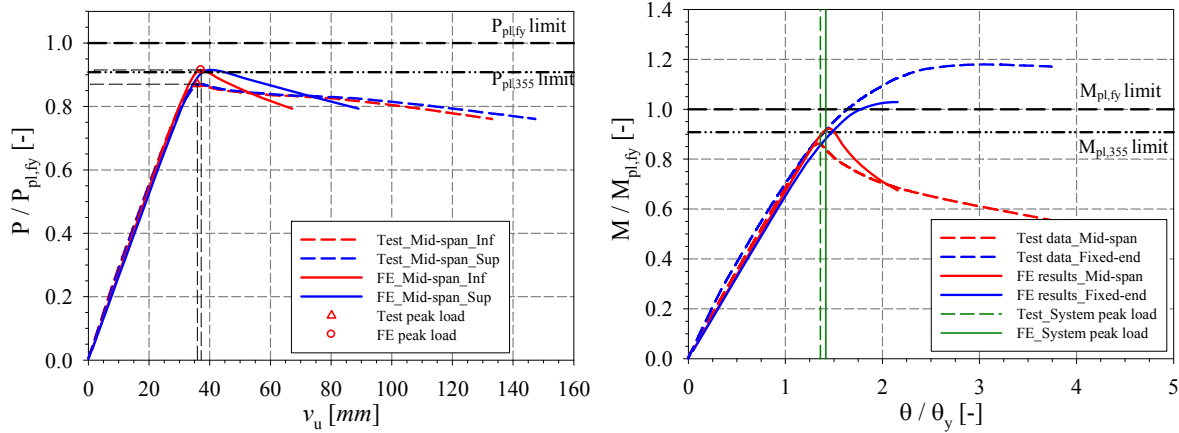
Figure 7 – SHS_180×6.3_PR_C test vs. F.E. analysis comparison

Results for all propped-cantilever centrally loaded specimens are summarized in Table 10. When comparing ultimate loads reached experimentally with their numerically-obtained counterparts, a very good correspondence is observed. On average, results diverged by 1% and a maximum deviation of only 5% is reached. A slightly higher divergence was noticed in term of rotations, as expected. These results demonstrate the capability of the numerical model to well predict the experimental behavior of propped-cantilever centrally loaded.

Table 10 – Numerical vs. experimental results for propped cantilever centrally-loaded tests

Test specimen	$P_{ult,FIL}/ P_{pl}$	$P_{ult,exp} / P_{ult,FE}$	θ_u / θ_y	$\theta_{u,exp} / \theta_{u,FE}$
	[-]	[-]	[-]	[-]
RHS_180×80×4.5_SS_3P	0.98	0.97	1.70	1.25
RHS_150×100×5_SS_3P	1.01	1.02	1.76	1.60
RHS_220×120×6.3_SS_3P	0.90	0.98	1.51	1.48
SHS_180×6.3_SS_3P	0.92	0.95	1.47	0.93
SHS_180×8_SS_3P	0.92	1.02	1.62	1.95

For propped-cantilever off-centrally loaded arrangements, similar conclusions could be drawn. Fig. 26 displays comparison curves for specimen SHS_180×6.3_PR_O; in terms of load-deflection as well as in moment-rotation curves, an excellent agreement is observed when comparing the stiffness of the beam response as well as the ultimate peak load, peak moment and deflection at peak load. These results highlight the capacity of the numerical model to well simulate the bending behavior of specimens. A faster unloading is noticeable in the numerical results, again to be associated with geometrical imperfection and to the modeling of load introduction. Table 11 summarizes numerical results and a comparison with test values. These values indicate the good prediction of the peak load by the numerical model and its accuracy.
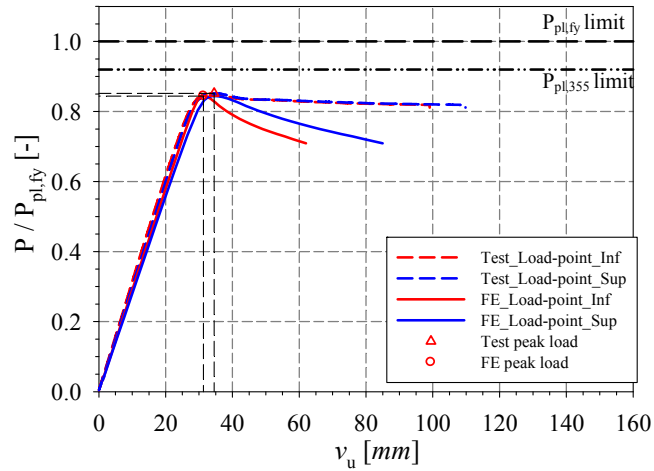
21

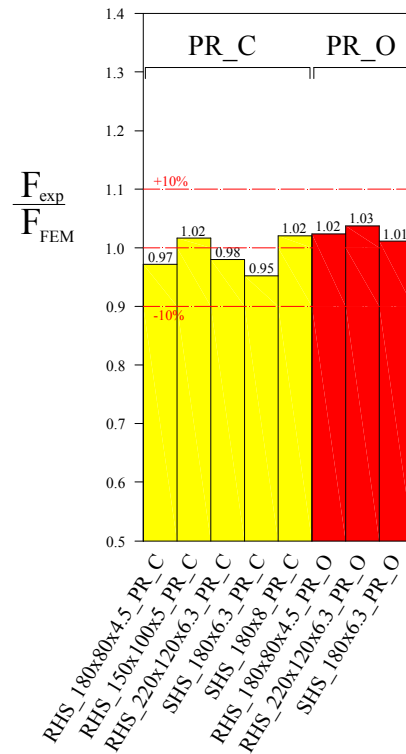Figure 8 – SHS_180×6.3_PR_O test vs. F.E. analysis comparison

Figure 27 – Graphical comparison of ultimate moments for propped-cantilever configurations

A graphical comparison of the ultimate loads from F.E. simulations to experimental ones is shown in Fig. 27, in which the red dashed lines indicate a deviation of +/- 10%. This summary of results indicate that numerical simulations represented well the real behavior of specimens.

Table 11 – Numerical vs. experimental results for propped cantilever off centrally-loaded tests

Test specimen	$P_{ult,FE} / P_{pl}$	$P_{ult,exp} / P_{ult,FE}$	θ_u / θ_y	$\theta_{u,exp} / \theta_{u,FE}$
	[-]	[-]	[-]	[-]
RHS_180×80×4.5_SS_3P	0.93	1.02	1.40	1.32
RHS_220×120×6.3_SS_3P	0.86	1.03	1.31	1.13
SHS_180×6.3_SS_3P	0.84	1.01	1.19	1.05

5. Conclusion and future research works

The present investigations concerned the possibility to resort to a new parameter called "cross-sectional" generalized slenderness λ_{CS} to serve as a measure of available ductility and be a convenient alternative to classical b / t ratios. In this respect, the paper first detailed a series of tests performed at the University of Applied Sciences of Western Switzerland – Fribourg. They basically consisted in bending tests, and included four different support and loading arrangements: (i) simply-supported 3-point tests, (ii) 4-point tests, (iii) indeterminate propped-cantilever centrally-loaded and (iv) propped-cantilever off-centrally loaded.

Besides, non-linear shell F.E. models were developed, and were shown capable of nicely replicating the experimental behavior of H.S.S. beams. Therefore, they can safely be substituted to physical tests and be subsequently used in extensive numerical studies.

Currently, such F.E. parametric studies are under development, and associated design requirements associating the generalized cross-section slenderness λ_{CS} to the available rotational capacity R_{cap} are being prepared.

References

[1] Galambos, T. V. (1968). "Deformation and energy absorption capacity of steel structures in the inelastic range," *Journal of Constructional Steel Research*.

[2] Yura, J., Galambos, T. V., Ravindra, M. (1978) "The bending resistance of steel beams." *Journal of the Structural Division*.

[3] Eurocode 3 Editorial Group (1989). "The b/t Ratios Controlling the Applicability of Analysis Models in Eurocode 3." *Document 5.02, Background Documentation to Chapter 5 of Eurocode 3*, Aachen University, Germany.

[4] Korol, R. M., Hudoba, J. (1972). "Plastic Behavior of Hollow structural sections.pdf." *Journal of the structural division*, American Society of Civil Engineers, Vol 98, No ST5, pp 1007-1023.

[5] Hasan, S. W., Hancock, G. J. (1989). "Plastic Bending Tests of Cold-Formed Rectangular Hollow Sections".

[6] Zhao, X. L., Hancock, G. J. (1991). "Tests to determine plate slenderness limits for cold-formed rectangular hollow sections of grade C450." *Journal of the Australian Steel Institute* 25(4):2-16.

[7] AS 4100 (1998). "Australian Standard AS 4100 Steel Structures".

[8] Kuhlmann, U. (1989). "Definition of flange slenderness limits on the basis of rotation capacity values," *J. Constr. Steel Res.*, vol. 14, no. 1, pp. 21–40.

[9] Neal, B. G. (1977). The plastic methods of structural analysis. London; New York: Chapman and Hall ; Wiley.

[10] Stranghoner, N., Sedlacek, G., Boeraeve, P. (1994). "Rotation requirement and rotation capacity of rectangular, square and circular hollow section beams." *Tubular structures VI*, Grundy, Holgate & Wong (eds).

[11] Lay, M. G., Galambos, T. V. (1967). "Inelastic beams under moment gradient." *Journal of the Structural Division*, ASCE.

[12] Kemp, A. R. (1984). "Slenderness limits normal to the plane of bending for beam-columns in plastic" *Journal of Constructional Steel Research* 4, 135-150.

[13] Kato, B. (1989). "Rotation capacity of H-section members as determined by local buckling." *Journal of Constructional Steel Research* 13, 95-109.

[14] Ziemian, R. D., McGuire, W., Deierlein, G. G. (1992). "Inelastic limit states design, Part I: Planar frame studies." *J. of St. Eng.*, ASCE, 118(9), pp. 2532–2549.

[15] Ricles, J. M., Sause, S., Green, P. S. (1998). "High-strength steel: implications of material and geometric characteristics on inelastic flexural behavior." *Eng. Struct.* 20 (4–6), 323–335..

[16] Wilkinson, T. (1999). "The Plastic Behaviour of Cold-Formed Rectangular Hollow Sections".

[17] EN 1993-1-1 (2005). "Eurocode 3: Design of steel structures, Part 1-1: General rules and rules for buildings".

[18] AISC (2005). "Specification for Structural Steel Buildings." American Institue of Steel Construction, Chicago, IL.

[19] Richard, J. (2014). "New design criterion to allow for a plastic analysis of rolled steel sections", *M.Sc. thesis*, University of Applied Sciences of Western Switzerland.

[20] Boissonnade, N., Nseir, J., Saloumi, E. (2013). "The Overall Interaction Concept: an Alternative Approach to the Stability and Resistance of Steel Sections and Members." *Proceedings of the Annual Stability Conference*, Structural Stability Research Council, St. Louis, Missouri.

[21] Saloumi, E. (2016). "Development of a new design method to define the rotation capacity of steel hollow sections", *Ph.D. thesis*.

[22] Greish and ULg, FINELg (1999). "Non linear finite element analysis software." University of Liege - Greisch Greisch Design Office.